Measurements of proton capture in the $A = 100$–110 mass region: Constraints on the ^{111}In$(\gamma, p)/(\gamma, n)$ branching point relevant to the γ process

O. Olivas-Gomez,[1,*] A. Simon,[1,†] O. Gorton,[2] J. E. Escher,[3] E. Churchman,[1,‡] P. Millican,[1] R. Kelmar,[1] C. S. Reingold,[1] A. M. Clark,[1] N. Cooper,[1,§] C. Harris,[4,5,6] S. L. Henderson,[1] S. E. Kelly,[1] F. Naqvi,[1,‖] A. Palmisano,[4,5,6] D. Robertson,[1] E. Stech,[1] A. Spyrou,[4,5,6] and W. P. Tan[1]

[1]*Department of Physics, The Joint Institute for Nuclear Astrophysics, University of Notre Dame, Indiana 46556-5670, USA*
[2]*San Diego State University, San Diego, California 92182, USA*
[3]*Lawrence Livermore National Laboratory, Livermore, California 94550, USA*
[4]*National Superconducting Cyclotron Laboratory, Michigan State University, East Lansing, Michigan 48824, USA*
[5]*Department of Physics and Astronomy, Michigan State University, East Lansing, Michigan 48824, USA*
[6]*Joint Institute for Nuclear Astrophysics, Michigan State University, East Lansing, Michigan 48824, USA*

(Received 28 February 2020; accepted 26 October 2020; published 24 November 2020)

The γ process is an explosive astrophysical scenario, which is thought to be the primary source of the rare proton-rich stable p nuclei. However, current γ-process models remain insufficient in describing the observed p-nuclei abundances, with disagreements up to two orders of magnitude. A sensitivity study has identified ^{111}In as a model-sensitive $(\gamma, p)/(\gamma, n)$ branching point within the γ process. Constraining the involved reaction rates may have a significant impact on the predicted p-nuclei abundances. Here we report on measurements of the cross sections for ^{102}Pd(p, γ) ^{103}Ag, ^{108}Cd(p, γ) ^{109}In, and ^{110}Cd(p, γ) ^{111}In reactions for proton laboratory energies 3–8 MeV using the high efficiency total absorption spectrometer and the γ-summing technique. These measurements were used to constrain Hauser-Feshbach parameters used in TALYS 1.9, which constrains the ^{111}In(γ, p) ^{110}Cd and ^{111}In(γ, n) ^{110}Ag reaction rates. The newly constrained reaction rates indicate that the ^{111}In $(\gamma, p)/(\gamma, n)$ branching point occurs at a temperature of 2.71 ± 0.05 GK, well within the temperature range relevant to the γ process. These findings differ significantly from previous studies and may impact the calculated abundances.

DOI: 10.1103/PhysRevC.102.055806

I. INTRODUCTION

The p nuclei are the proton-rich stable nuclei between ^{74}Se through ^{196}Hg. As a group they are the rarest of all stable nuclei with abundances typically two to three orders of magnitude lower than other stable isotopes of the same element [1]. Unlike most nuclei heavier than iron, which can be made through sequential neutron captures in the s and r processes, the p nuclei are shielded from β decay by the valley of stability, and, thus, it was determined that an alternative mechanism is needed [2]. Presently, the origin of the p nuclei remains an elusive mystery.

The most favored and thoroughly investigated model for the production of the p nuclei is known as the γ process [3]. The γ process is based on explosive astrophysical scenarios in which at temperatures between 2.0–3.0 GK photodisintegration reactions, [i.e., (γ, p), (γ, n), and (γ, α)], on preexisting r- and s-process seed nuclei can produce most of the p nuclei. This process is illustrated in Fig. 1 for the $A = 100$–110 mass region.

For many years, the primary astrophysical site for the γ process was thought to primarily occur within the oxygen neon rich layers of a massive star undergoing core-collapse type-II supernova [4]. Type-II supernova based γ-process models are mildly successful in predicting most of the solar p-nuclei abundances within about a factor of 3. However, there are serious deficiencies, especially in the molybdenum ruthenium region where the solar abundances are underpredicted by up to 2 orders of magnitude [5]. Thus, there could be several independent astrophysical scenarios contributing to the production of the p nuclei (see Ref. [6] and the references therein). For example, recent advances in simulations have demonstrated that the γ process can also occur within the carbon-rich layers of a white dwarf undergoing a type-Ia supernova [7].

Therefore, although the γ process may be the primary candidate for the production of the p nuclei, it is not clear to what extent each astrophysical site contributes to the p-nuclei abundances. One of the major factors hindering progress is due to uncertainties of the associated nuclear physics. To

*ogomez@nd.edu
†anna.simon@nd.edu
‡Current address: University of North Carolina at Chapel Hill, NC 27599, USA.
§Deceased.
‖Current address: Department of Physics and Astrophysics, University of Delhi, Delhi 110007, India.

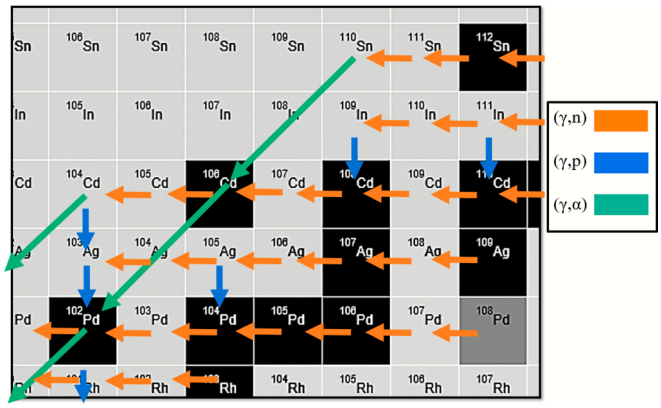

FIG. 1. The γ-process reaction flow for the $A = 100$–110 mass region where photodisintegration reactions on seed nuclei can produce the p nuclei (shown here ^{102}Pd, ^{106}Cd, ^{108}Cd, and ^{112}Sn). Colored arrows indicate the dominant photodisintegration reaction. Isotopes with two outgoing arrows are branching points; at a critical temperature, one reaction rate will become stronger than the other.

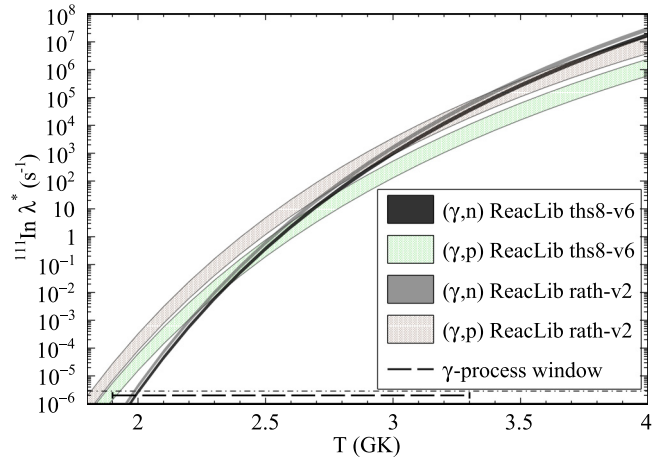

FIG. 2. Stellar photodisintegration reaction rates for ^{111}In. The light shaded bands are (γ, p) rates taken from the JINA REACLIB database [13]. The labels refer to the version of NON-SMOKER used. The uncertainty of the reaction rates makes it unclear at what temperature (γ, n) begins to dominate (γ, p), which can have a significant impact on γ-process model predictions of p-nuclei abundances.

better understand the γ process and the contributions coming from different astrophysical sites, it is imperative to constrain the nuclear input, which is the focus of this paper.

Modeling of the γ process requires input of thousands of nuclear reaction rates, which requires knowledge of the cross section within the appropriate Gamow energy window for each reaction. However, most of these cross sections have not been experimentally measured and, thus, rely on theoretical calculations. The calculations are performed using the Hauser-Feshbach statistical reaction formalism [8], which is implemented in reaction model codes, such as TALYS [9] and NON-SMOKER [10,11]. However, due to the lack of experimental data, parameters inherent to the Hauser-Feshbach theory are poorly constrained. For example, proton and neutron capture/emission reaction rates calculated by NON-SMOKER have uncertainties of about a factor of 2 [10].

This becomes an issue primarily when the (γ, n) and (γ, p) reaction rates for an isotope are comparable in magnitude within the γ-process temperature window. As illustrated in Fig. 1, the γ process proceeds through a sequence of (γ, n) reactions, shifting the abundances to the proton-rich side of stability. At some point along a chain of isotopes, the (γ, p) or (γ, α) rate becomes stronger than that of neutron emission, and the mass flow branches into another isotopic chain. These are known as branching points, and establishing their locations is crucial for accurate modeling of the γ process. However, due to the reaction rate uncertainties, there is an ambiguity in the location of several branching points, and consequently, in the reaction flow of several mass regions which may have a significant impact on the predicted p-nuclei abundances.

In one particular case, a sensitivity study [12] has identified ^{111}In as a potential $(\gamma, p)/(\gamma, n)$ model-sensitive branching point within the γ process. This is demonstrated in Fig. 2, which shows the stellar photodisintegration rates for ^{111}In, taken from the JINA REACLIB database [13]. The (γ, p) and (γ, n) rates (labeled tsh8-v6 and rath-v2) are based on two versions of the NON-SMOKER code [11,13] with tsh8-v6 being the most recent. The (γ, p) rates from these two versions differ by about a factor of 5. The inconsistencies between these two rates, coupled with the uncertainty of the reaction rates, make it unclear at what temperature (γ, n) begins to dominate. If the ths8-v6 version is correct, it could be between 2.3 and 3 GK. On the other hand, rath-v2 predicts the branching point above 3 GK and possibly outside the γ-process window.

Above the branch-point temperature, $^{111}\mathrm{In}(\gamma, n)^{110}\mathrm{In}$ begins to dominate, and the reaction flow would feed into ^{108}Cd through the series of reactions: $^{110}\mathrm{In}(\gamma, n)\,^{109}\mathrm{In}(\gamma, p)\,^{108}$Cd (see Fig. 1). Below the branch-point temperature however, $^{111}\mathrm{In}(\gamma, p)\,^{110}$Cd would dominate, feeding into ^{110}Cd. So, if the branch-point temperature is determined to be within the γ-process temperature window, the abundance ratio of ^{108}Cd to ^{110}Cd would be sensitive to temperature, which would be a useful metric in constraining the seed distribution and/or astrophysical conditions necessary for the γ process.

Thus, the purpose of this paper is to reduce the nuclear uncertainties of γ-process models by constraining the $^{111}\mathrm{In}(\gamma, n)\,^{110}\mathrm{In}$ and $^{111}\mathrm{In}(\gamma, p)\,^{110}$Cd reaction rates. This constrains the ^{111}In $(\gamma, p)/(\gamma, n)$-temperature branching point, improving our understanding of the reaction flow in this mass region.

To achieve this goal, the cross sections for $^{108}\mathrm{Cd}(p, \gamma)\,^{109}\mathrm{In}$, and $^{110}\mathrm{Cd}(p, \gamma)\,^{111}\mathrm{In}$ were measured between laboratory energies 3 and 8 MeV, which covers most of the Gamow window for each reaction. By measuring (p, γ) cross sections of nuclei near ^{111}In, the measurements can be used to constrain the Hauser-Feshbach parameters and, consequentially, constrain the inverse reaction rates of interest. In addition, the $^{102}\mathrm{Pd}(p, \gamma)$ cross section was also measured throughout a similar energy range. The inclusion of this reaction, being a lower mass relative to the other

TABLE I. Summary of the reactions measured in this paper with respective energy ranges in the laboratory frame. Also included are the target thickness and isotopic enrichment.

Reaction	E_p (MeV)	Thickness (mg/cm^2)	^{102}Pd (%)	^{104}Pd (%)	^{105}Pd (%)	^{106}Pd (%)	^{108}Pd (%)	^{110}Pd (%)
^{102}Pd$(p,\gamma)^{103}$Ag	4–8	1.575(20)	78.18(5)	5.45(2)	6.20(2)	5.45(2)	3.49(2)	1.23(2)
			^{106}Cd (%)	^{106}Cd (%)	^{110}Cd (%)	^{111}Cd (%)	^{112}Cd (%)	^{113}Cd (%)
^{108}Cd$(p,\gamma)^{109}$In	3.5–7	2.0962(35)	0.877(5)	69.33(5)	6.69(1)	5.59(2)	6.16(2)	3.90(2)
^{110}Cd$(p,\gamma)^{111}$In	3–6	2.142(12)	$\leqslant$0.01	0.02(1)	97.36(2)	0.94(2)	0.94(1)	0.27(1)

two nuclei, helped limit the bias when constraining the set of Hauser-Feshbach parameters used in describing similar reactions in the $A = 100$–110 mass region to be discussed later.

The remainder of the paper is organized as follows: first the experimental setup is presented, followed by a brief review of the high efficiency total absorption spectrometer (HECTOR) and the γ-summing technique in Sec. II. Next, the data analysis technique is discussed in Sec. III, followed by a presentation of the measured (p,γ) cross sections in Sec. IV. Finally, a discussion of the constrained Hauser-Feshbach parameters and constrained ^{111}In$(\gamma,n)^{110}$In and ^{111}In$(\gamma,p)^{110}$Cd reaction rates are presented in Sec. V.

II. EXPERIMENTAL METHOD

The measurements were performed at the University of Notre Dame Nuclear Science Laboratory (NSL) [14] using the 10-MV FN Tandem Van de Graaf accelerator to produce protons with laboratory-frame energies E_p between 3 and 8 MeV. The energy was determined through a nuclear magnetic resonance probe and selected via an analyzing magnet, resulting in a beam with an energy spread of approximately 15 keV. The protons then impinged on isotopically enriched self-supported foil targets of ^{102}Pd, ^{108}Cd, and ^{110}Cd.

For each measurement, the target was mounted to a target holder and placed at the center of the HECTOR. The HECTOR is an array of 16 NaI(Tl) crystals with two photomultiplier tubes attached to each segment which allows for detection of γ rays. Through the center of the array is a 60-mm bore radius allowing clearance for the beam pipe and target. A detailed description of the HECTOR and its data-acquisition system is given in Ref. [15].

The incident beam current was measured by electrically isolating the beam pipe surrounding the target which acted as a Faraday cup. The current from the beam pipe was then collected and recorded using a charge integrator. The beam current ranged between 5 and 100 nA and was varied to maximize the count rate while minimizing the detection dead time. The detector dead time was kept below 1% throughout the experiment.

The target thicknesses were measured via Rutherford backscattering spectroscopy performed at the NSL. A 3.2-MeV proton and 4-MeV α beam were scattered off each target and detected with silicon detectors placed at 135° and 145° with respect to the incident beam. The scattering data for each angle and incident beam was then fitted using the SIMNRA software package [16]. The average thicknesses and uncertainties are reported in Table I along with their isotopic enrichment provided by the target manufacturer.

III. DATA ANALYSIS

For the (p,γ) reactions considered in this paper, a compound nucleus is formed with excitation energy given by

$$E_\Sigma = E_{\text{c.m.}} + Q, \tag{1}$$

where $E_{\text{c.m.}}$ is the center-of-mass energy and Q is the Q value of the reaction. The nucleus then deexcites via emission of one or several γ rays as it transitions to the ground state (g.s.). With its almost 4π-angular coverage, the HECTOR is able to absorb the entire γ cascade, allowing for the energies of each emitted γ ray to be summed into a single peak. This is known as the sum peak, which is centered at energy E_Σ. The number of counts in this sum peak is related to the total (p,γ) cross

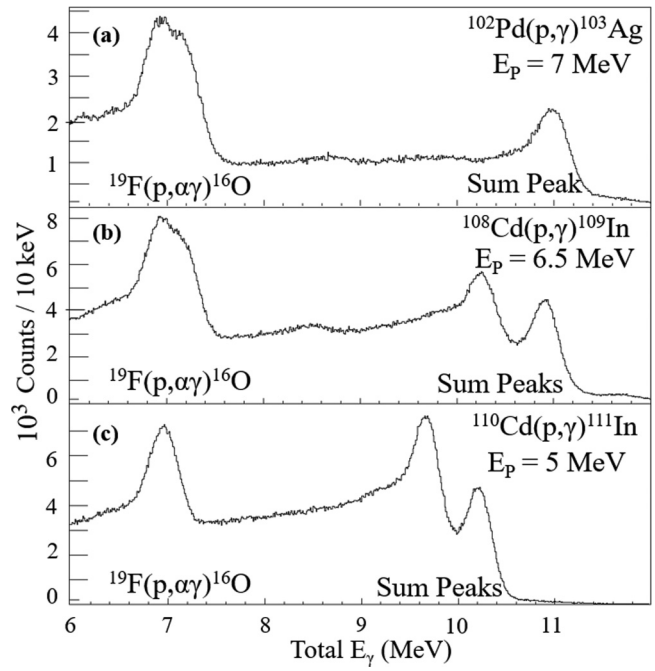

FIG. 3. Sum spectra (before background subtraction) for proton capture reactions on (a) ^{102}Pd, (b) ^{108}Cd, and (c) ^{110}Cd. Note that for the cadmium reactions due to the long-lived metastable (m.s.) state for the compound nuclei ^{109}In and ^{111}In, there are two resolvable sum peaks.

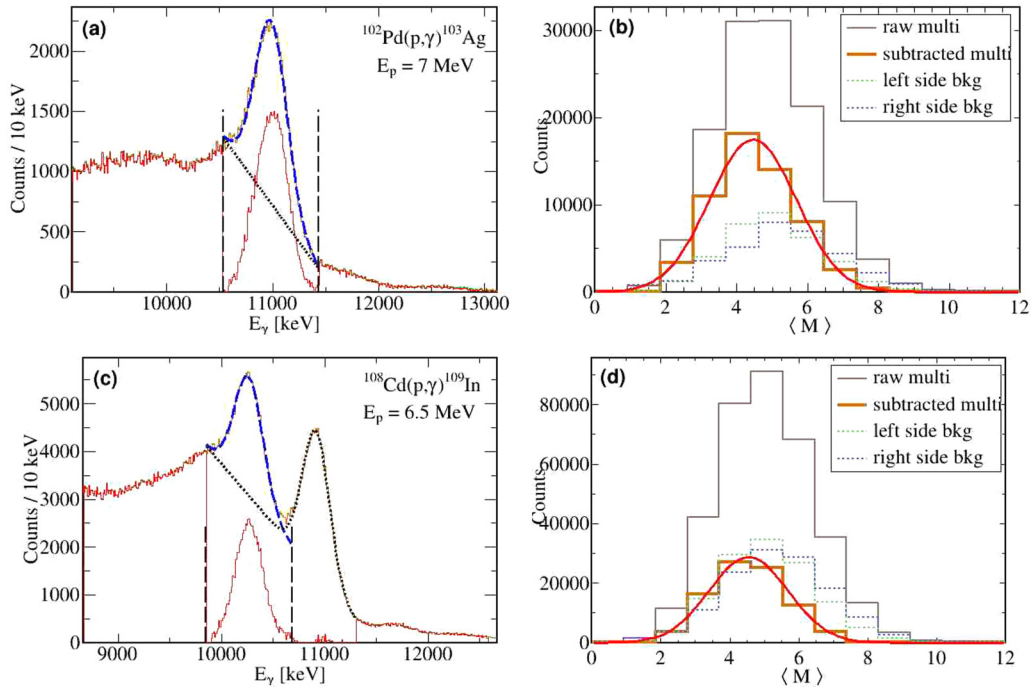

FIG. 4. Fitting of the ^{102}Pd$(p,\gamma)^{103}$Ag [panels (a) and (b)] and ^{108}Cd$(p,\gamma)^{109}$In [panels (c) and (d)] sum peaks. For panels (a) and (c), the purple curves highlight the Gaussian fits to the sum peak whereas the dashed black curve is the background to be subtracted. For ^{108}Cd and ^{110}Cd, the two sum peaks are fitted simultaneously, but whereas determining the counts of one sum peak, the other is treated as background. The subtracted sum peak to be integrated is shown in orange whereas the three standard deviation windows are marked with vertical black dashes. Panels (b) and (d) show the segment-multiplicity distributions from events within the integrated region of the sum peak. These are adjusted by background subtracting segment multiplicities sampled from energies 25–100 keV below and above the gate windows (vertical dashed lines).

section through the relation,

$$\sigma_{\text{total}} = \frac{N_\Sigma}{N_b\, N_t\, \varepsilon_\Sigma}, \tag{2}$$

where N_Σ is the number of counts within the sum peak, N_b is the total number of incident beam particles, N_t is the areal target density, and ε_Σ is the summing efficiency. This method of simultaneously measuring all γ-ray energies is known as the γ-summing technique [17].

A typical sum spectrum before background subtraction, with 10-keV binning, is shown in Fig. 3. From top to bottom are the ^{102}Pd$(p,\gamma)^{103}$Ag at $E_p = 7$ MeV, ^{108}Cd$(p,\gamma)^{109}$In at $E_p = 6.5$ MeV and ^{110}Cd$(p,\gamma)^{111}$In at $E_p = 5$ MeV, respectively. For all three reactions, the compound nucleus can decay into a metastable state which is long lived compared to the 100-ns time window used to record events to the digital acquisition system. This results in multiple sum peaks within the spectrum. However, the $1/2^-$ metastable state for ^{103}Ag is only 135 keV above the ground state; therefore, the second peak was not resolvable within the resolution of the detector. For the ^{109}In and ^{110}In cases, the $1/2^-$ metastable states are 650 and 537 keV, respectively, above the ground state and were clearly resolvable. In either case, all resolvable sum peaks needed to be integrated to determine the total (p,γ) cross section.

The largest source of contamination in each spectrum came from fluorine impurities in the targets which resulted in ^{19}F$(p,\alpha\gamma)^{16}$O peaks between 6 and 7 MeV. This set the lower-energy limit for which each reaction could be measured; beyond this point the sum peak could no longer be distinguished from the contamination peak. In addition, for the ^{102}Pd(p,γ), and ^{108}Cd(p,γ) spectra, there is a small contribution to the background on the higher-energy side of the sum peaks due to proton capture on heavier isotopes of palladium and cadmium, respectively. The ^{110}Cd target is more highly enriched than the other targets, so the higher-energy background is smaller in comparison.

The first step of the analysis was proper subtraction of the background under the sum peak, which includes room and cosmic-ray background as well as events corresponding to incomplete summation. For ^{102}Pd, a procedure consistent with previous applications of the γ-summing technique [15] was used. A normalized background run with no beam on target was first subtracted from the spectrum, followed by a fitting of a Gaussian with a linear background to the sum peak. This is demonstrated in the top-left panel of Fig. 4 for $E_p = 7$ MeV. The fitted Gaussian is highlighted in purple whereas the background to be subtracted is marked by a dashed black line. The orange peak just below is the resultant sum peak after subtracting the linear background, which was then integrated between three standard deviations about the sum peak. The integration region is marked by the black dashed vertical lines.

For ^{108}Cd (shown in the bottom-left panel of Fig. 4 for $E_p = 6.5$ MeV) the procedure is similar. However, since there are two sum peaks, both peaks were fitted simultaneously with

a linear background. Each peak was then integrated separately, so both the linear background and the opposite sum peak is subtracted before integrating the sum peak of interest. In the figure, the metastable peak is being integrated (left peak), so the ground-state sum peak is treated as background and subtracted.

The summing efficiency, in general, depends both on the total energy of the sum peak as well as the individual γ-ray energies of the γ cascades. For the compound nuclei ^{103}Ag, ^{109}In, and ^{111}In, a complete level scheme is not known, nor does the HECTOR have the energy resolution to isolate each individual γ-ray energy. However, previous studies of γ-summing detectors have demonstrated that by measuring the average number of segments that fired $\langle M \rangle$ for events within the sum peak, the efficiency can be estimated, even without complete knowledge of the level schemes and/or branching ratios [15,18].

Therefore, $\langle M \rangle$ was determined by collecting segment multiplicities for events gated within the sum-peak integration region, and fitting a Gaussian to the resulting distribution (see the top-right and bottom-right panels of Fig. 4). The experimentally determined $\langle M \rangle$ was then compared to those generated from GEANT4 [19] simulations of random γ cascades with the same sum-peak energy. However, the experimental $\langle M \rangle$ had to be adjusted due to background events under the sum peak, which cannot be accounted for in the GEANT4 simulations. Therefore, a background $\langle M \rangle$ was sampled for events 25–100 keV below and above the gated region, in order to estimate the background. These events are plotted and labeled as "left side bkg" and "right side bkg" in Fig. 4. The background $\langle M \rangle$ was then scaled to the ratio of the sum peak to the linear background and then subtracted from the experimental $\langle M \rangle$ distribution. The final result is plotted and labeled as "subtracted multi" in Fig. 4.

In order to quantify the uncertainties in the cross-sectional measurements, the uncertainty of each term in Eq. (2) was added in quadrature. The uncertainties of both the number of beam particles and the target density were taken to be 5%. The uncertainty in the sum peak integral was taken as the square root of the total number of counts from the sum peak and subtracted background. This was typically less than 10% for all measurements. Overall, the efficiency of the sum peak is the largest source of uncertainty, ranging from 10 and 20% in relative uncertainty. The uncertainty in the center-of-mass energy is a combination of the 15-keV spread of the beam energy with the energy loss in the target. The energy loss was calculated using the SRIM framework [20].

IV. RESULTS

The three measured (p, γ) cross sections are shown in Fig. 5. In addition, theoretical calculations from the NON-SMOKER code are also plotted for comparison as they are commonly used for astrophysical calculations. These NON-SMOKER cross sections correspond to the rath-v2 version, which were obtained from the NON-SMOKER web site [21]. Experimental cross-sectional values and uncertainties are listed in Table II for palladium and Table III for the cadmium isotopes.

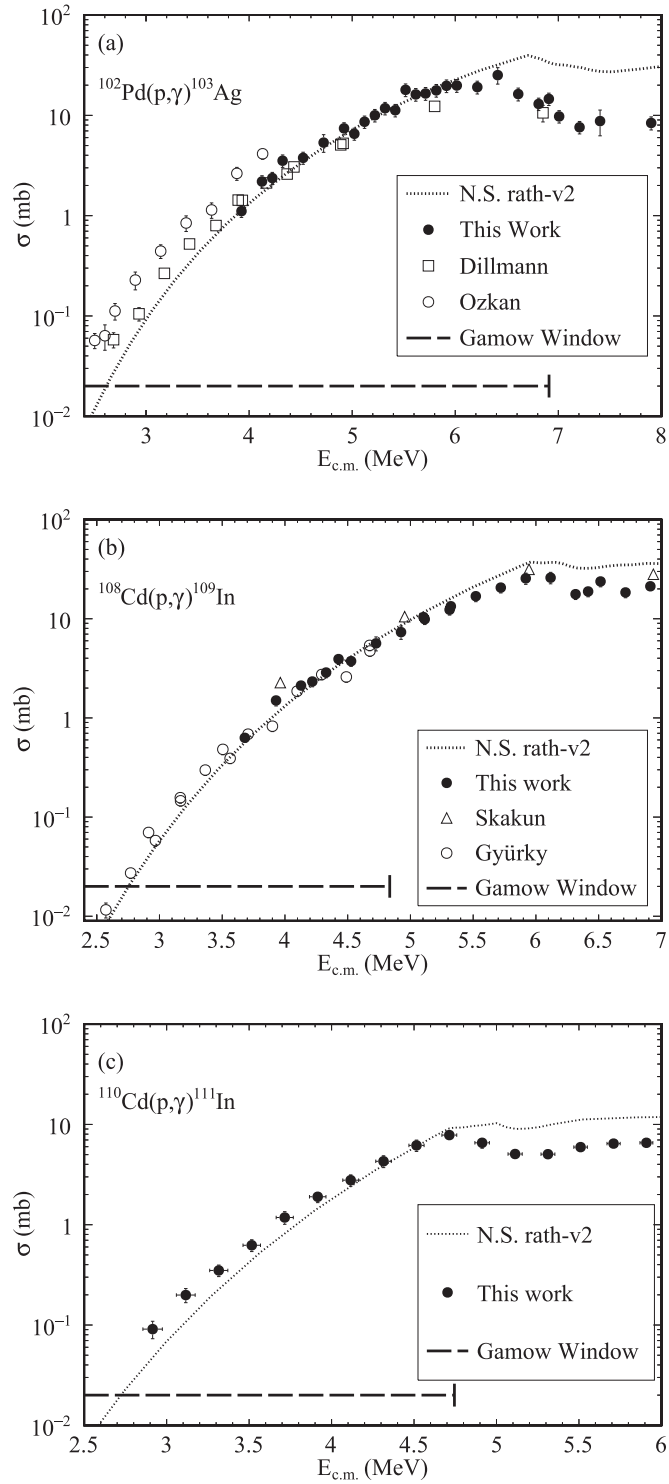

FIG. 5. Experimentally measured cross sections for the ^{102}Pd(p, γ) ^{103}Ag, ^{108}Cd(p, γ) ^{109}In, and ^{110}Cd(p, γ) ^{111}In reactions. Theoretical predictions from the NON-SMOKER code are shown for comparison. The dashed line marks the Gamow window for each reaction.

For ^{102}Pd(p, γ) ^{103}Ag, there are two previous measurements in the literature by Dillmann *et al.* [22] and Özkan *et al.* [23]. Although there is a consistent discrepancy between these two measurements by approximately a factor of 2, our

TABLE II. Cross sections measured for the ^{102}Pd$(p,\gamma)^{103}$Ag reaction. Energy is reported in the center-of-mass frame.

$E_{\text{c.m.}}$ (MeV)	σ (mb)	$E_{\text{c.m.}}$ (MeV)	σ (mb)
3.926 ± 0.038	1.11 ± 0.15	5.712 ± 0.031	16.5 ± 2.4
4.125 ± 0.037	2.19 ± 0.31	5.816 ± 0.030	17.8 ± 2.6
4.225 ± 0.036	2.37 ± 0.33	5.915 ± 0.030	19.7 ± 2.8
4.325 ± 0.035	3.53 ± 0.50	6.015 ± 0.030	19.9 ± 2.9
4.524 ± 0.035	3.77 ± 0.52	6.214 ± 0.029	19.1 ± 2.9
4.722 ± 0.034	5.4 ± 1.1	6.412 ± 0.028	25.2 ± 4.7
4.921 ± 0.033	7.4 ± 1.0	6.611 ± 0.028	16.3 ± 2.4
5.021 ± 0.033	6.55 ± 0.90	6.809 ± 0.028	13.0 ± 1.8
5.120 ± 0.032	8.6 ± 1.2	6.908 ± 0.028	14.6 ± 2.1
5.220 ± 0.032	10.0 ± 1.4	7.008 ± 0.027	9.8 ± 1.4
5.319 ± 0.032	11.8 ± 1.7	7.206 ± 0.027	7.6 ± 1.1
5.418 ± 0.031	11.3 ± 1.6	7.405 ± 0.026	8.8 ± 2.5
5.518 ± 0.031	18.0 ± 2.6	7.901 ± 0.026	8.4 ± 1.3
5.617 ± 0.031	16.2 ± 2.3		

measurements are in good agreement with those of Dillmann *et al.*

For ^{108}Cd$(p,\gamma)^{109}$In, there are also two previous measurements in the literature by Gyürky *et al.* [24] and Skakun and Batij [25]. Our measurements are in good agreement with both measurements. ^{110}Cd$(p,\gamma)^{111}$In was measured for the first time and, therefore, has no experimental comparison.

Comparing the NON-SMOKER predictions to the experimental measurements, it is in good agreement with the ^{108}Cd measurements. However, it tends to underpredict the cross sections at lower energies and overestimate it at higher energies above the neutron separation threshold. This is most likely due to improper constraints on the level density and γ-strength function, which are Hauser-Feshbach parameters to be discussed in detail in the following section.

V. DISCUSSION

A. Hauser-Feshbach cross sections

The conditions necessary for the application of the statistical Hauser-Feshbach model, such as high excitation energies involving many overlapping energy states, are readily satisfied for many of the nuclear reactions within the γ process [10]. In this picture, a target nucleus in state μ captures an incident particle α, forming a compound nucleus which, subsequently, decays to final-state ν with emission of particle β. Following the discussion of [10], the cross section is given by

$$\sigma_{(\alpha,\beta)}^{\mu,\nu} = \frac{\pi\hbar^2/(2mE_{\text{c.m.}})}{(2J^{\mu}+1)(2J_{\alpha}+1)} \sum_{J,\pi}(2J+1)\frac{T_{\alpha}^{\mu}(J,\pi)T_{\beta}^{\nu}(J,\pi)}{\sum_{\beta',\nu'} T_{\beta'}^{\nu'}(J,\pi)}, \tag{3}$$

where m is the reduced mass, J is the spin, and π is parity. T_{α}^{μ} is the transmission coefficient for the formation of the compound nucleus from entrance state μ. Similarly, T_{β}^{ν} is the transmission coefficient for the decay of the compound nucleus to final-state ν. The denominator is a normalization term, considering all possible exit channels that are energetically accessible.

TABLE III. Cross sections measured for the ^{108}Cd$(p,\gamma)^{109}$In and ^{110}Cd$(p,\gamma)^{111}$In reaction. The second column is for capture to the first excited state, the third column is for capture to the ground state, and the fourth column is the total cross section. Energy is reported in the center-of-mass frame.

$E_{\text{c.m.}}$ (MeV)	$\sigma_{\text{m.s}}$ (mb)	$\sigma_{\text{g.s}}$ (mb)	$\sigma_{(p,\gamma)}$ (mb)
	^{108}Cd		
3.680 ± 0.038	0.293 ± 0.050	0.341 ± 0.052	0.634 ± 0.072
3.929 ± 0.037	0.74 ± 0.13	0.76 ± 0.12	1.50 ± 0.18
4.128 ± 0.036	1.02 ± 0.17	1.10 ± 0.17	2.12 ± 0.24
4.218 ± 0.035	1.09 ± 0.19	1.24 ± 0.19	2.33 ± 0.27
4.328 ± 0.035	1.35 ± 0.23	1.52 ± 0.24	2.87 ± 0.33
4.427 ± 0.035	1.80 ± 0.31	2.12 ± 0.33	3.92 ± 0.46
4.527 ± 0.034	1.67 ± 0.28	2.07 ± 0.32	3.74 ± 0.43
4.726 ± 0.033	2.50 ± 0.63	3.14 ± 0.65	5.65 ± 0.91
4.925 ± 0.033	3.17 ± 0.75	4.15 ± 0.85	7.3 ± 1.1
5.104 ± 0.032	4.58 ± 0.78	5.82 ± 0.91	10.4 ± 1.2
5.114 ± 0.032	4.36 ± 0.77	5.54 ± 0.87	9.9 ± 1.2
5.312 ± 0.031	5.35 ± 0.94	7.0 ± 1.1	12.3 ± 1.5
5.322 ± 0.031	5.63 ± 0.95	7.7 ± 1.2	13.4 ± 1.5
5.521 ± 0.031	7.4 ± 1.3	9.5 ± 1.6	16.9 ± 2.0
5.720 ± 0.030	8.8 ± 1.5	11.9 ± 1.9	20.6 ± 2.4
5.919 ± 0.030	11.0 ± 2.2	14.6 ± 2.4	25.6 ± 3.3
6.117 ± 0.029	11.1 ± 2.4	14.8 ± 2.5	25.9 ± 3.4
6.316 ± 0.029	7.4 ± 1.3	10.3 ± 1.6	17.7 ± 2.1
6.416 ± 0.028	8.3 ± 1.4	10.6 ± 1.7	18.9 ± 2.2
6.515 ± 0.028	10.5 ± 1.8	13.2 ± 2.1	23.8 ± 2.8
6.714 ± 0.028	8.0 ± 1.3	10.5 ± 1.7	18.4 ± 2.2
6.912 ± 0.027	9.1 ± 1.4	12.2 ± 2.0	21.3 ± 2.4
	^{110}Cd		
2.915 ± 0.059	0.061 ± 0.015	0.030 ± 0.010	0.091 ± 0.018
3.116 ± 0.057	0.123 ± 0.025	0.076 ± 0.021	0.199 ± 0.032
3.316 ± 0.055	0.212 ± 0.040	0.138 ± 0.024	0.350 ± 0.046
3.516 ± 0.053	0.373 ± 0.072	0.251 ± 0.044	0.624 ± 0.084
3.716 ± 0.052	0.70 ± 0.14	0.48 ± 0.10	1.18 ± 0.17
3.916 ± 0.050	1.11 ± 0.20	0.79 ± 0.14	1.90 ± 0.24
4.116 ± 0.048	1.60 ± 0.29	1.19 ± 0.21	2.78 ± 0.36
4.315 ± 0.047	2.43 ± 0.46	1.86 ± 0.35	4.29 ± 0.58
4.515 ± 0.046	3.46 ± 0.64	2.72 ± 0.48	6.18 ± 0.80
4.714 ± 0.045	4.39 ± 0.65	3.44 ± 0.51	7.83 ± 0.83
4.913 ± 0.044	3.77 ± 0.63	2.79 ± 0.43	6.56 ± 0.77
5.113 ± 0.043	2.94 ± 0.42	2.13 ± 0.31	5.07 ± 0.53
5.312 ± 0.042	2.90 ± 0.43	2.14 ± 0.32	5.05 ± 0.54
5.510 ± 0.041	3.43 ± 0.51	2.51 ± 0.37	5.94 ± 0.64
5.710 ± 0.040	3.72 ± 0.55	2.71 ± 0.40	6.44 ± 0.68
5.909 ± 0.039	3.73 ± 0.56	2.84 ± 0.43	6.56 ± 0.70

Regarding the experimental cross-sectional measurements, μ corresponds to the ground state and the emission particle is a γ ray. However, a single final-state ν is not measured, but rather all final states due to the 4π-summing nature of the HECTOR. Thus, the experimental cross sections are related to Eq. (3) through a summation over the final-states ν. Since the excitation energy of the compound nucleus is well into the continuum, the summation is customarily divided into two terms: One summing over the γ transitions into known discrete states up to some energy threshold, beyond which

the summation becomes an integral over the continuum states with respect to energy using a level density. Thus,

$$\sum_{\nu} T_{\gamma}^{\nu} = \sum_{i=0}^{\omega} T_{\gamma}^{i} + \int_{E_{\omega}}^{E_{\Sigma}} \sum_{J',\pi'} T_{\gamma}(E, J', \pi')\rho(E, J', \pi')dE \tag{4}$$

where ω is the number of known discrete states, E_{ω} is the energy of the highest known state, and ρ is the nuclear level density which describes the number of states with spin J' and parity π' at excitation energy E.

Thus, the important quantities for calculating a cross section from Eqs. (3) and (4) are the particle, γ-transmission coefficients, and the nuclear level density (NLD). The particle transmission coefficients are calculated by an optical model potential (OMP); the γ-transmission coefficients are given by a γ-strength function (γSF); the NLD is typically modeled based on variations of superfluid or Fermi-gas models.

B. Constraining the NLD and γSF

Each of the models underlying the Hauser-Feshbach cross sections, (i.e., the OMP, γSF, and NLD), has associated with it an uncertainty which contributes to the overall uncertainty of the cross section. For phenomenological models, there are several parameters which are typically fit to nuclear data. For example, the Kopecky-Uhl generalized Lorentzian γSF (KU-γSF) [26], which is a parametrization of a Lorentzian representation of the giant dipole resonance (GDR), depends on the strength, centroids, and widths of the $E1$ and $M1$ GDR. The Gilbert-Cameron NLD model (GC-NLD), which is the combination of a constant-temperature model with a Fermi-gas model at higher temperatures [27], depends on an energy-dependent level-density parameter a. The values of these parameters depend on the nuclear structure of the nuclei participating in the reaction; when there is no experimental information, they are estimated from systematics and/or extrapolated.

Using the (p, γ) cross sections measured in this paper, statistical parameter estimation within γSF and NLD models were carried out using TALYS 1.9. TALYS 1.9 utilizes the most recently updated nuclear database [28] and combines several scattering and nuclear structure models into a unified statistical framework. Like NON-SMOKER, TALYS is able to calculate cross sections and reaction rates under the Hauser-Feshbach formalism.

For the NLD, the GC-NLD was used. The internal parameters constrained were the asymptotic level-density parameter $\tilde{a}$, and the level-density damping parameter γ of the three nuclei in the proton-entrance, neutron-exit, and γ-exit channels of each reaction. For example, in the ^{110}Cd$(p, \gamma)^{111}$In reaction, ^{110}Cd, ^{110}In, and ^{111}In are considered.

For the γSF, $E1$ transitions were calculated using the KU-γSF. The internal parameters constrained were the centroid, width, and strength of the $E1$ GDR. The $M1$ transition were calculated using the Brink-Axel Lorentzian (BA-γSF) [29,30]. Two $M1$ peaks were considered, and the internal parameters constrained were the centroids, strengths, and widths of these peaks. Higher-order transitions were left as the TALYS default, which is discussed in Ref. [31].

TABLE IV. Posterior distribution values for parameters within the GC-NLD based off the MCMC procedure. $\tilde{a}$ is the asymptotic-level-density parameter, and γ is the level-density-damping parameter. The values with a 16, 50, and 84 subscript refer to the percentile values of the distribution, while the values with a T subscript refer to the TALYS 1.9 default.

	$\tilde{a}_T$	$\tilde{a}_{16}$	$\tilde{a}_{50}$	$\tilde{a}_{84}$	γ_T	γ_{16}	γ_{50}	γ_{84}
^{102}Pd	13.24	10.17	14.84	21.05	0.093	0.067	0.087	0.109
^{103}Ag	13.35	14.78	15.44	16.22	0.092	0.063	0.084	0.105
^{102}Ag	13.24	8.08	11.20	14.43	0.093	0.064	0.092	0.115
^{108}Cd	13.89	8.19	12.80	17.58	0.091	0.071	0.101	0.123
^{109}In	14.00	15.94	16.87	17.70	0.091	0.041	0.081	0.103
^{108}In	13.89	10.66	14.22	17.53	0.091	0.065	0.093	0.121
^{110}Cd	14.11	8.89	12.79	16.00	0.090	0.036	0.073	0.101
^{111}In	14.22	13.10	14.23	16.45	0.090	0.049	0.083	0.113
^{110}In	14.11	10.33	14.62	17.42	0.090	0.064	0.088	0.110

Regarding the OMP, the Koning and Delaroche OMP (KD-OMP) [32] was used for protons and neutrons. For the α OMP—the TALYS default—the α potential of Avrigeanu *et al.* [33] was chosen, which is consistent with the recommendation by Ref. [34] for the same mass region. The parameters within these models were not varied and kept as the TALYS default.

In total, 15 parameters for each reaction were constrained; these parameters were found to be the dominant factors affecting the cross-sectional predictions. To constrain the parameters, a Markov chain Monte Carlo (MCMC) algorithm was used to sample the posterior probability distribution, which was found by combining prior knowledge of the parameters with new knowledge given by the experimental measurements described in this paper. This is accomplished with Bayes' theorem,

$$P(\Theta|\Sigma) = \frac{L(\Sigma|\Theta)\, p(\Theta)}{p(\Sigma)}, \tag{5}$$

where Θ is the set of model parameters ($\tilde{a}$, γ, etc.) and Σ is the set of experimental cross-sectional measurements (previous measurements in the literature are not included). $p(\Theta)$ is the joint prior probability distribution of the parameters, which was taken to be uniform to obtain an unbiased posterior. $p(\Sigma)$ is a normalization constant. $L(\Sigma|\Theta)$ is the likelihood function, which is defined to be a multivariate normal distribution, with means equal to the measured cross-sections σ and a diagonal covariance matrix with elements equal to the square of the experimental uncertainties,

$$L(\Sigma|\Theta) \propto \exp\left[-\sum_{i\in\Sigma}\left(\frac{\sigma_{\mathrm{exp}} - \sigma_{\mathrm{th}}(\Theta)}{\delta\sigma_{\mathrm{exp}}}\right)^2\right]. \tag{6}$$

A Metropolis Hastings algorithm [35] serves as the MCMC sampler. For each reaction, 15 independent chains of 1500 steps were computed. The first 500 steps of each chain were considered "burn in," and discarded. In total, the posterior distribution for each reaction contains 15 000 samples. The constrained parameter values are tabulated in Tables IV and V.

TABLE V. Posterior distribution values for parameters within the γSF based off the MCMC procedure. E gives the centroid in MeV, σ gives the strength in millibars, and Γ gives the width in MeV of the GDR. The $E1$ transitions are calculated from the KU-γSF; the $M1$ peaks are calculated from the BA-γSF. The values with a 16, 50, and 84 subscript refer to the percentile values of the distribution. The values with a T subscript refer to the TALYS 1.9 default for these models. TALYS does not include a second $M1$ peak, thus, no value is given.

	Centroid (MeV)				Strength (mb)				Width (MeV)			
	E_T	E_{16}	E_{50}	E_{84}	σ_T	σ_{16}	σ_{50}	σ_{84}	Γ_T	Γ_{16}	Γ_{50}	Γ_{84}
					$E1$ peak							
^{103}Ag	16.17	17.70	21.82	25.40	221.3	121.0	185.6	235.0	5.29	3.39	4.49	6.37
^{109}In	15.96	14.21	16.60	19.40	239.6	131.5	191.3	253.4	5.16	3.96	5.29	6.85
^{111}In	15.89	12.19	15.68	20.61	245.1	122.3	217.9	262.1	5.12	3.93	5.38	7.10
					$M1$ primary peak							
^{103}Ag	8.75	8.69	10.30	12.26	0.72	0.83	1.41	1.76	4.00	1.86	3.73	4.87
^{109}In	8.58	8.20	10.17	13.02	0.70	0.91	1.33	1.82	4.00	1.69	3.20	4.63
^{111}In	8.53	5.88	8.34	10.75	0.69	0.79	1.13	1.71	4.00	2.21	3.57	6.06
					$M1$ secondary peak							
^{103}Ag		2.80	3.06	3.33		0.72	1.04	1.35		0.77	1.23	1.72
^{109}In		4.69	5.45	5.99		0.29	0.68	0.99		0.72	1.09	1.50
^{111}In		3.35	4.08	5.43		0.51	0.99	1.24		0.81	1.16	1.53

Once the joint posterior probability distribution $P(\Theta|\Sigma)$ is obtained, a distribution of cross-sectional predictions can be calculated by sampling from $P(\Theta|\Sigma)$. The results of this are shown in the left panels of Fig. 6. The band represents a 68% confidence interval, whereas central values are taken as the median. As a comparison, the TALYS 1.9 calculations using the default parameters values for the same NLD and γSF are shown as well. The results are a significant improvement over the TALYS 1.9 default and NON-SMOKER models as the predictions are in good agreement with the experimental data throughout the energy range measured. In a similar fashion, the inverse cross section and reaction rates of interest can also be calculated by sampling from $P(\Theta|\Sigma)$, which is discussed in Sec. V.

C. Microscopic NLD and γSF models

In the previous section, the internal parameters within phenomenological models were constrained, resulting in predictions that agree well with experiment within uncertainties. However, as previously mentioned, the uncertainties of the internal parameters grow with extrapolation from experimental data. In addition to determining the best-constrained reaction rates, it is also beneficial to develop a model for the mass region that can be used for nearby nuclei where there is still little to no experimental data. For this, we turn to microscopic γSF and NLD models.

Microscopic models tend to be less accurate, but are more robust, capable of describing a small mass region with less need for experimental data for recalibration of their internal parameters. However, there are many microscopic γSFs and NLDs available within TALYS, and it is unclear which combination best describes the region of interest; random combinations of these models vary the cross-sectional predictions by over a factor of 10.

Thus, every combination possible for microscopic γSF and NLD models available within TALYS 1.9 was tested. Within TALYS 1.9, there are three microscopic NLDs and six microscopic γSFs for a total of 18 combinations; each model is listed in Table VI. For the OMP, the KD-OMP, and the semimicroscopic Jeukenne-Lejeune-Mahaux OMP (JMP-OMP) [42] were tested for protons and neutrons. Like the previous method, the α OMP remained as the TALYS default.

The total number of combinations tested was then 36. From each combination, theoretical cross sections for each energy measured in this paper were calculated and compared to the experimental values. Unlike the previous method, the default parameters of the microscopic models were not changed. In order to determine the best combination, the χ^2 value for each model was computed, which is equal to the argument in the exponent of Eq. (6), taking σ_{th} as the model prediction, and σ_{exp} as the experimental cross section for a given energy.

The model combination with the smallest χ^2 for each individual reaction is labeled as Local and is plotted as a solid line on the right-hand panels of Fig. 6 for that reaction. The other reactions are plotted as a dashed line for comparison. From the 36 model combinations, the KD-OMP had a lower χ^2 compared to its JMP-OMP counterpart. From the 18 combinations that used the KD-OMP, model 4-3 was found to have the smallest χ^2 across all three reactions. The two numbers correspond to the NLD-γSF used. This model combination is labeled as Global and is shown as a solid red line in all three plots.

Figure 7 shows the relative differences between the microscopic model predictions with the experimental measurements. Although the local models tend to fit their reaction rather well, the discrepancies tend to grow when compared to experimental measurements of the other reactions. The Global 4-3 combination in contrast, on average deviates from experiment within 50% for all three reactions. Therefore, the

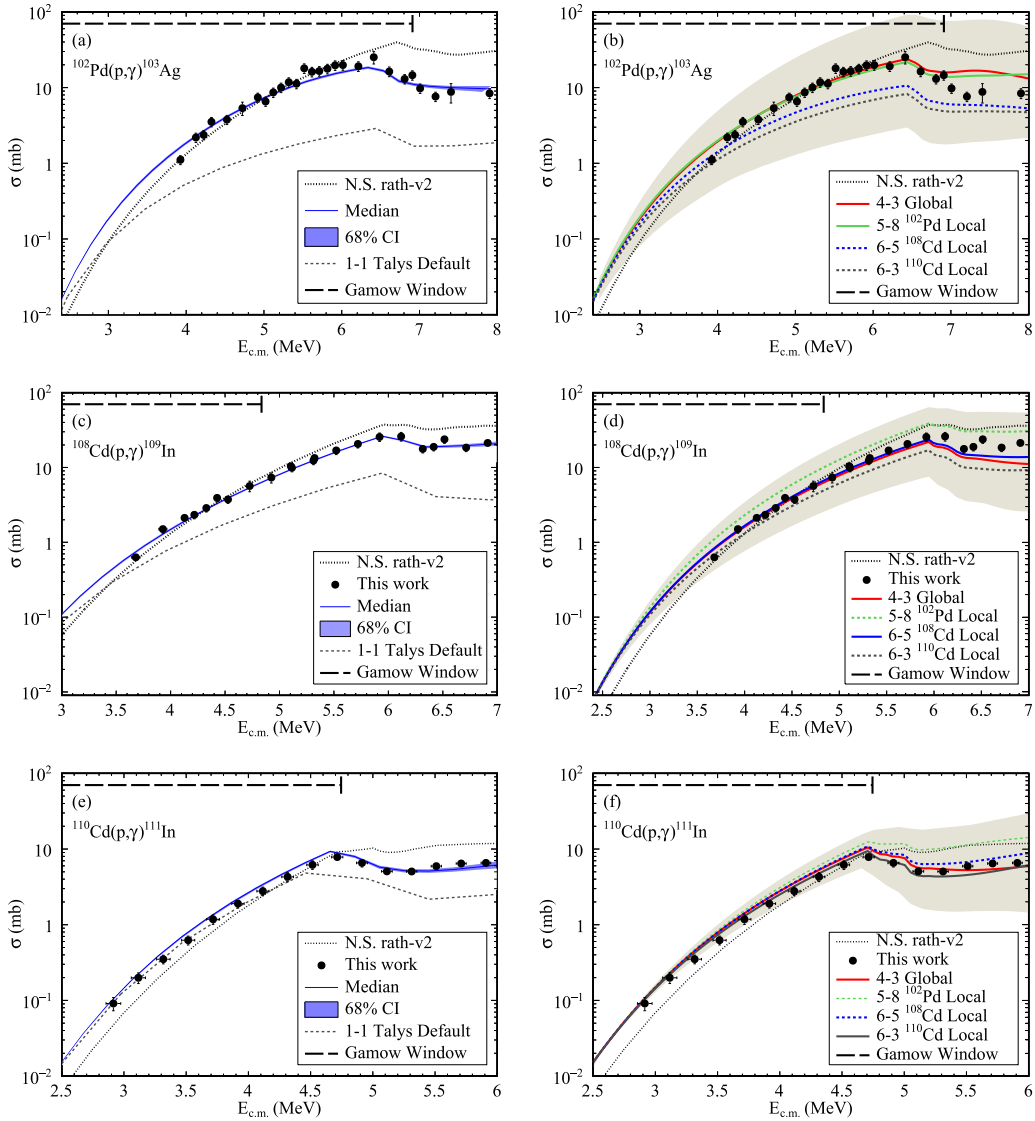

FIG. 6. Constraining of Hauser-Feshbach statistical parameters used to predict cross sections. The left panels show the MCMC-fitted result based off constrained parameters within the KU-γSF and GC-NLD models. The solid blue line is the median prediction whereas the band represents a 68% confidence interval. For the panels on the right-hand side, predictions based off different combinations of microscopic NLD and γSF are shown. The shaded band represents the total range of predictions from all microscopic model combinations available in TALYS 1.9. The combination that best fits all three reactions from this work is labeled "Global" whereas the combination that best fits a single reaction is labeled as "Local." The number notation represents NLD and γSF model number consistent with the notation used in the TALYS 1.9 manual [31].

KD-OMP, the Skyrme force calculated NLD from Goriely's and $E1$ transitions calculated by a γSF based off the Hartree-Fock BSC tables model combination is recommended for predicting cross sections and reaction rates for nuclei in the $A = 100$–110 mass region. Although not as accurate as the constrained phenomenological model, it is still an improvement over the previous NON-SMOKER model. This is particularly true at lower energies of the Gamow window where NON-SMOKER tends to underestimate the (p, γ) cross section. Therefore, this model can serve as a useful extrapolation for calculating cross sections and reaction rates for nearby nuclei where there is still no experimental data.

The microscopic and phenomenological models discussed in this section were also compared to the experimental partial cross sections (capture to the ground state and metastable state) for ^{108}Cd and ^{110}Cd, which is shown in Fig. 8. The models are in good agreement with the measurements within the uncertainties.

D. Reaction rates

Calculation of the photodisintegration decay rates requires integration of the cross section folded over the photon number

TABLE VI. Microscopic NLD and γSF available within TALYS 1.9. The numbering notation is consistent with the TALYS 1.9 manual [31]. The microscopic γSFs calculate the dominant $E1$ transitions; $M1$ and all other higher-order transitions are calculated using the BA-γSF.

NLD	
ldmodel 4:	Skyrme force from Goriely's tables [36].
ldmodel 5:	Skyrme force from Hilaire's combinatorial tables [37].
ldmodel 6:	Temperature-dependent Hartree-Fock-Bolgubyubov (HFB), Gogny force from Hilaire's combinatorial tables [38].
γSF	
Strength 3:	Hartree-Fock BCS tables [28].
Strength 4:	HFB tables [28].
Strength 5:	Goriely's hybrid tables [39].
Strength 6:	Goriely's temperature dependent HFB [38].
Strength 7:	temperature-dependent relativistic mean field [40].
Strength 8:	Gogny D1M HFB and quasiparticle random-phase approximation [41].

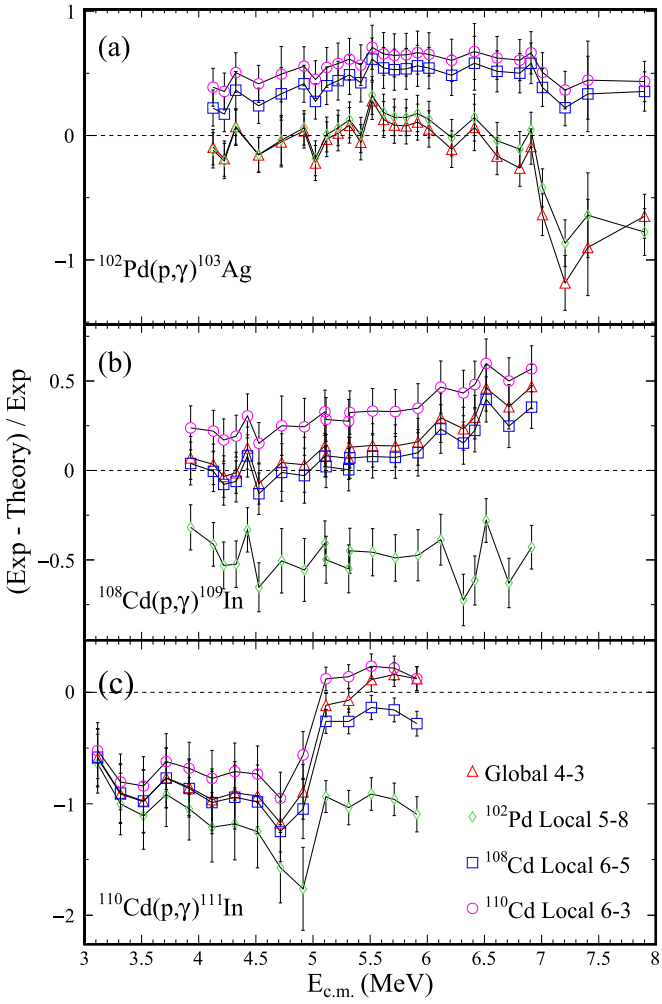

FIG. 7. Relatives differences in cross sections between the experimental values and the microscopic-model predictions for each of the three reactions. Error bars are propagated from the experimental uncertainties.

density with respect to the incident γ-ray energy,

$$\lambda_{(\gamma,\beta)}(T) = \frac{1}{\pi^2 c^2 \hbar^3} \int_0^\infty \frac{E_\gamma^2}{e^{E_\gamma/kT} - 1} \sigma_{(\gamma,\beta)}(E_\gamma) dE_\gamma, \quad (7)$$

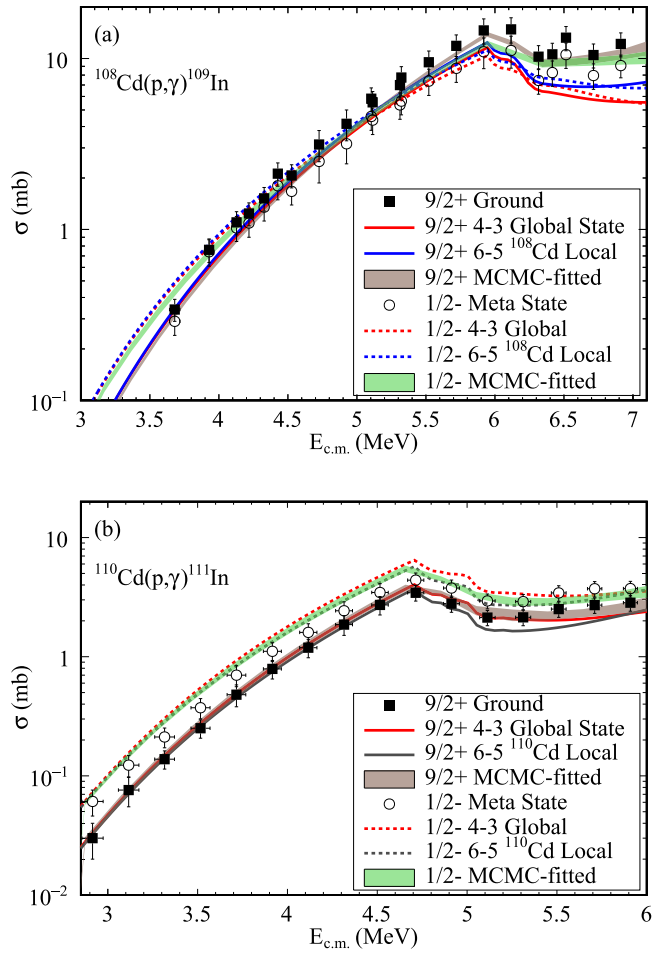

FIG. 8. Comparison of the MCMC-fitted GC-NLD, KU-γSF, and microscopic models to the experimentally measured partial cross sections of (a) ^{108}Cd and (b) ^{110}Cd.

TABLE VII. Recommended (γ, p) and (γ, n) stellar photodissociation decay rates for ^{103}Ag, ^{109}In, and ^{111}In. Rates are based on the MCMC-fitted model with values corresponding to the median of the distribution calculated by TALYS 1.9. Subscripts and superscripts give the 16th and 84th percentile, respectively.

	λ^* (s^{-1})					
T (GK)	^{103}Ag$(\gamma, p)^{102}$Pd	^{103}Ag$(\gamma, n)^{102}$Ag	^{109}In$(\gamma, p)^{108}$Cd	^{109}In$(\gamma, n)^{108}$In	^{111}In$(\gamma, p)^{110}$Cd	^{111}In$(\gamma, n)^{110}$In
1.0	$1.50^{1.52}_{1.45} \times 10^{-17}$		$1.43^{1.43}_{1.42} \times 10^{-19}$		$4.16^{4.19}_{4.13} \times 10^{-24}$	
1.5	$1.74^{1.76}_{1.66} \times 10^{-7}$		$8.58^{8.64}_{8.50} \times 10^{-9}$		$1.74^{1.75}_{1.72} \times 10^{-11}$	$4.65^{5.24}_{3.84} \times 10^{-15}$
2.0	$4.80^{4.90}_{4.55} \times 10^{-2}$	$4.95^{5.22}_{4.67} \times 10^{-8}$	$5.56^{5.63}_{5.48} \times 10^{-3}$	$2.81^{2.93}_{2.69} \times 10^{-7}$	$5.67^{5.72}_{5.58} \times 10^{-5}$	$2.67^{3.03}_{2.19} \times 10^{-6}$
2.5	$1.45^{1.48}_{1.36} \times 10^{2}$	$1.66^{1.76}_{1.57} \times 10^{-2}$	$2.88^{2.93}_{2.82} \times 10^{1}$	$7.96^{8.32}_{7.61} \times 10^{-2}$	$7.86^{7.94}_{7.68} \times 10^{-1}$	$4.45^{5.06}_{3.63} \times 10^{-1}$
3.0	$4.04^{4.15}_{3.81} \times 10^{4}$	$8.39^{8.88}_{7.84} \times 10^{1}$	$1.18^{1.20}_{1.15} \times 10^{4}$	$3.64^{3.81}_{3.47} \times 10^{2}$	$6.00^{6.09}_{5.81} \times 10^{2}$	$1.43^{1.62}_{1.16} \times 10^{3}$
3.5	$2.72^{2.81}_{2.57} \times 10^{6}$	$3.80^{4.01}_{3.53} \times 10^{4}$	$1.03^{1.06}_{1.00} \times 10^{6}$	$1.53^{1.60}_{1.46} \times 10^{5}$	$7.77^{7.93}_{7.41} \times 10^{4}$	$4.64^{5.28}_{3.77} \times 10^{5}$
4.0	$7.26^{7.52}_{6.88} \times 10^{7}$	$3.75^{3.96}_{3.48} \times 10^{6}$	$3.22^{3.32}_{3.08} \times 10^{7}$	$1.41^{1.47}_{1.34} \times 10^{7}$	$3.08^{3.18}_{2.84} \times 10^{6}$	$3.52^{4.00}_{2.81} \times 10^{7}$
5.0	$8.62^{9.08}_{8.05} \times 10^{9}$	$2.28^{2.42}_{2.10} \times 10^{9}$	$3.70^{4.13}_{3.25} \times 10^{9}$	$6.51^{6.99}_{5.92} \times 10^{9}$	$4.84^{5.47}_{3.79} \times 10^{8}$	$1.34^{1.53}_{0.956} \times 10^{10}$
6.0	$2.17^{2.41}_{1.92} \times 10^{11}$	$1.45^{1.60}_{1.25} \times 10^{11}$	$5.97^{7.93}_{4.47} \times 10^{10}$	$2.46^{3.08}_{1.94} \times 10^{11}$	$1.10^{1.61}_{0.599} \times 10^{10}$	$5.28^{6.77}_{3.20} \times 10^{11}$
7.0	$1.94^{2.38}_{1.56} \times 10^{12}$	$2.23^{2.63}_{1.59} \times 10^{12}$	$3.10^{5.44}_{1.98} \times 10^{11}$	$2.22^{3.25}_{1.51} \times 10^{12}$	$7.92^{18.5}_{2.77} \times 10^{10}$	$5.23^{8.18}_{2.52} \times 10^{12}$
8.0	$8.41^{11.9}_{5.73} \times 10^{12}$	$1.25^{1.64}_{0.696} \times 10^{13}$	$9.17^{25.4}_{4.80} \times 10^{11}$	$9.33^{15.4}_{5.58} \times 10^{12}$	$2.75^{13.3}_{0.667} \times 10^{11}$	$2.26^{4.36}_{0.961} \times 10^{13}$
9.0	$2.25^{3.71}_{1.28} \times 10^{13}$	$3.53^{5.26}_{1.52} \times 10^{13}$	$2.00^{8.67}_{0.769} \times 10^{12}$	$2.53^{4.58}_{1.38} \times 10^{13}$	$6.38^{61.3}_{1.11} \times 10^{11}$	$5.94^{13.7}_{2.41} \times 10^{13}$
10.0	$4.37^{8.15}_{2.13} \times 10^{13}$	$6.40^{10.6}_{2.12} \times 10^{13}$	$3.63^{20.5}_{0.958} \times 10^{12}$	$5.04^{9.82}_{2.46} \times 10^{13}$	$1.14^{18.8}_{0.146} \times 10^{12}$	$1.13^{3.15}_{0.441} \times 10^{14}$

where E_γ is the energy of the incident γ ray and $\sigma_{(\gamma,\beta)}$ is the cross section for the photodisintegration reaction to exit channel β. However, in stellar interiors, nuclei exist not only in their ground states, but also in excited states in thermal equilibrium. Therefore, a calculation of the stellar photodisintegration decay rate, which accounts for thermally accessible excited states, is needed. The stellar photodisintegration rate is given by

$$\lambda^*_{(\gamma,\beta)}(T) = \frac{\sum_\mu \lambda^\mu_{(\gamma,\beta)}(T) e^{-E^\mu_x/kT}}{\sum_\mu (2J^\mu + 1) e^{-E^\mu_x/kT}}, \tag{8}$$

where $\lambda^\mu_{(\gamma,\beta)}$ is the photodisintegration rate of a nuclei in state μ with excitation energy E^μ_x and spin J.

Using TALYS 1.9 the stellar (γ, p) and (γ, n) decay rates for the inverse reactions measured in this paper were calculated for temperatures between 0.001 and 10 GK. The rates are tabulated in Table VII, which are based off the MCMC-fitted model where each calculation was performed using parameters sampled from the posterior distribution. Stellar decay rates below 1 GK in general were below TALYS' precision, and, therefore, have been omitted from the table. The ^{111}In stellar photodissociation decay rates based off the MCMC-fitted model along with the global and local ^{110}Cd microscopic model are plotted in Fig. 9. These rates are in good agreement, within uncertainties, with the predictions from the REACLIB tsh8-v6.

Despite two different approaches used to constrain the Hauser-Feshbach theory, the stellar (γ, p) rates are in good agreement with one another. There is, however, some slight variation between model predictions of the stellar (γ, n) rates. This is to be expected since the reactions were constrained based off (γ, p) cross-sectional measurements. Furthermore, the MCMC-fitted approach alters the level density of the neutron exit channel.

In the bottom panel of Fig. 9, the ratios of the stellar (γ, p) to (γ, n) decay rates are shown. The ratio of rates from the REACLIB ths8-v6 has an uncertainty estimated at about a factor of 3, which is shown as a gray band. Within this uncertainty band, the MCMC-fitted KU-γSF, GC-NLD model constrains the branch-point temperature to 2.71 ± 0.05 GK. Although the line thickness of the microscopic-model rate ratios are aesthetic for easier distinguishing, the band of the MCMC-fitted model represents a 68% percentile of the posterior distribution. The ^{110}Cd micromodel is in good agreement whereas the Global model predicts the branch-point temperature at around 2.6 GK. This discrepancy is somewhat expected as, in general, the Global model will be less accurate but serve as a better estimation for other reaction rates in the $A = 100$–110 mass region.

Based on our results, the branch-point temperature is indeed within the γ-process temperature window, and the abundance ratio of ^{108}Cd – ^{110}Cd will be temperature sensitive. In addition, it can be seen that the global-microscopic model gives similar predictions to the MCMC-fitted model, helping to validate it as a model useful in investigating other reaction rates in the same mass region.

VI. CONCLUSION

In an effort to better model the γ process and potentially mitigate discrepancies of the predicted p-nuclei abundances, the ^{111}In$(\gamma, p)^{110}$Cd and ^{111}In$(\gamma, n)^{110}$In reaction rates were constrained, constraining the

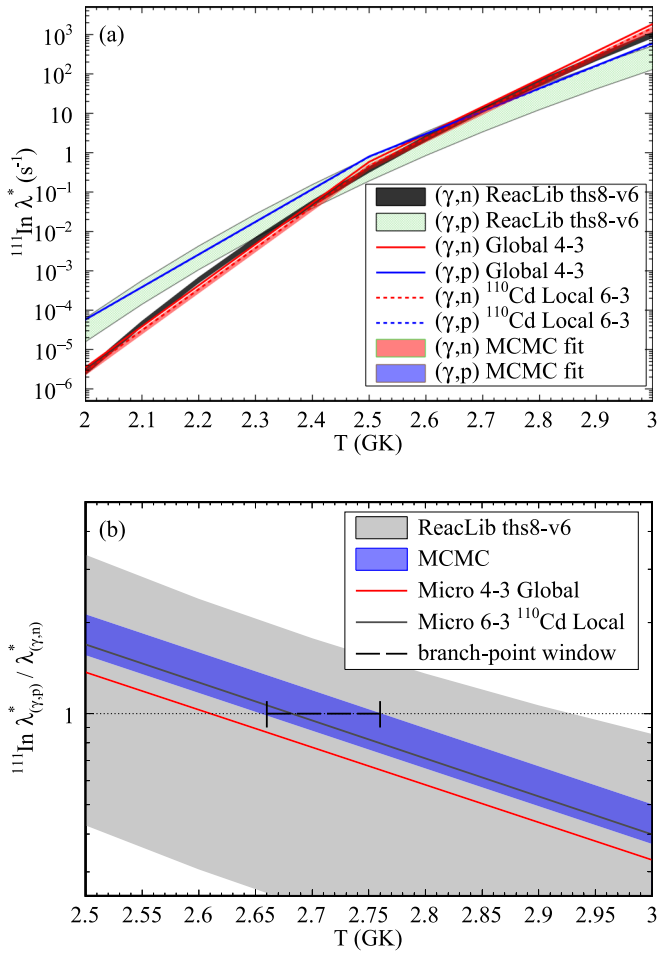

FIG. 9. (a) shows predicted stellar photodissociation decay rates for ^{111}In based off MCMC-fitted and microscopic γSF and NLD models. The previous rates based off of REACLIB-V6 are plotted for comparison. (b) plots the ratio of the $(\gamma, p)/(\gamma, n)$ stellar decay rates. Band thickness of the MCMC-fitted (KU-γSF and GC-NLD) reflects a 68% confidence interval band.

temperature of the ^{111}In$(\gamma, p), (\gamma, n)$ branching point. This was achieved by measuring the cross sections for ^{102}Pd$(p, \gamma)^{103}$Ag, ^{108}Cd$(p, \gamma)^{109}$In, and ^{110}Cd$(p, \gamma)^{111}$In, and then using the measurements to constrain γSF and NLD models used in Hauser-Feshbach theory within TALYS 1.9. In constraining these models we have adopted two different approaches: In one approach parameters within phenomenological models, such as the KU-γSF and GC-NLD were constrained through a MCMC sampling algorithm; another approach investigated various combinations of microscopic γSF and NLD, identifying the combination which best describes the experimental measurements. We recommend using the global-microscopic combination as discussed in Sec. V for estimating cross sections and reaction rates for proton and neutron reactions in the $A = 100$–110 mass region where there are no experimental measurements. Both methods give similar predictions for the ^{111}In$(\gamma, p)^{110}$Cd and ^{111}In$(\gamma, n)^{110}$In reaction rates.

In conclusion, with a few stable-target experiments, the ^{111}In$(\gamma, p)/(\gamma, n)$ branch-point temperature for which only previously the lower limit of 2.3 GK was established has been constrained to 2.71 ± 0.05 GK; this is a reduction of over a factor of 30. However, the uncertainties presented are only systematic as there may be additional uncertainties inherit to the TALYS code which are difficult to quantify. Based on our results, above the branching-point temperature ^{108}Cd will be fed through ^{109}In, whereas below ^{110}Cd will be fed through ^{111}In. This may have an impact on the predicted abundances of these isotopes as well on the lighter p nuclei, warranting further investigation. Furthermore, future cross-sectional measurements to constrain other model-dependent γ-process branching points are desirable as constraining the nuclear input will likely continue to provide further insight and constraints into the astrophysical conditions necessary to produce the p nuclei.

ACKNOWLEDGMENTS

This work was supported by the National Science Foundation under Grants No. PHY-1614442, No. PHY-1713857 (NSL), and No. PHY-1430152 (JINA Center for the Evolution of the Elements). A part of this work was performed under the auspices of the U.S. Department of Energy by Lawrence Livermore National Laboratory under Contract No. DE-AC52-07NA27344 with support from LDRD Project No. 19-ERD-017, the HEDP summer student program, and the Seaborg Institute.

[1] E. Anders and N. Grevesse, Geochim. Cosmochim. Acta **53**, 197 (1989).
[2] E. M. Burbidge, G. R. Burbidge, W. A. Fowler, and F. Hoyle, Rev. Mod. Phys. **29**, 547 (1957).
[3] S. E. Woosley and W. M. Howard, Astrophys. J., Suppl. Ser. **36**, 285 (1978).
[4] M. Arnould and S. Goriely, Phys. Rep. **384**, 1 (2003).
[5] M. Rayet, N. Prantzos, and M. Arnould, Astron. Astrophys. **227**, 271 (1990).
[6] T. Rauscher, N. Dauphas, I. Dillmann, C. Frohlich, Z. Fülöp, and G. Gyürky, Rep. Prog. Phys. **76**, 66201 (2013).
[7] C. Travaglio, F. K. Röpke, R. Gallino, and W. Hillebrandt, Astrophys. J. **739**, 93 (2011).
[8] W. Hauser and H. Feshbach, Phys. Rev. **87**, 366 (1952).
[9] A. Koning and D. Rochman, Nucl. Data Sheets **113**, 2841 (2012).
[10] T. Rauscher and F. Thielemann, At. Data Nucl. Data Tables **75**, 351 (2000).
[11] T. Rauscher and F. Thielemann, At. Data Nucl. Data Tables **79**, 47 (2001).
[12] T. Rauscher, Phys. Rev. C **73**, 015804 (2006).
[13] R. H. Cyburt, A. M. Amthor, R. Ferguson, Z. Meisel, K. Smith, S. Warren, A. Heger, R. D. Hoffman, T. Rauscher, A. Sakharuk,

H. Schatz, F. K. Thielemann, and M. Wiescher, Astrophys. J., Suppl. Ser. **189**, 240 (2010).
[14] Nuclear Science Laboratory, http://www.isnap.nd.edu (2019).
[15] C. S. Reingold, O. Olivas-Gomez, A. Simon, J. Arroyo, M. Chamberlain, J. Wurzer, A. Spyrou, F. Naqvi, A. C. Dombos, A. Palmisano, T. Anderson, A. M. Clark, B. Frentz, M. R. Hall, S. L. Henderson *et al.*, Eur. Phys. J. A **55**, 77 (2019).
[16] M. Mayer, Max-Planck-Instiut für Plasmaphysik Report No. IPP 9/113, 1997.
[17] A. Spyrou, H.-W. Becker, A. Lagoyannis, S. Harissopulos, and C. Rolfs, Phys. Rev. C **76**, 015802 (2007).
[18] A. Simon, S. Quinn, A. Spyrou, A. Battaglia, I. Beskin, A. Best, B. Bucher, M. Couder, P. DeYoung, X. Fang, J. Görres, A. Kontos, Q. Li, S. Liddick, A. Long *et al.*, Nucl. Instrum. Methods Phys. Res., Sect. A **703**, 16 (2013).
[19] J. Allison, K. Amako, J. Apostolakis, P. Arce, M. Asai, T. Aso, E. Bagli, A. Bagulya, S. Banerjee, G. Barrand, B. Beck, A. Bogdanov, D. Brandt, J. Brown, H. Burkhardt *et al.*, Nucl. Instrum. Methods Phys. Res., Sect. A **835**, 186 (2016).
[20] J. Ziegler, M. Ziegler, and J. Biersack, Nucl. Instrum. Methods Phys. Res., Sect. B **268**, 1818 (2010).
[21] T. Raushcher, NON-SMOKER Database, https://nucastro.org/nonsmoker.html (2015).
[22] I. Dillmann, L. Coquard, C. Domingo-Pardo, F. Käppeler, J. Marganiec, E. Uberseder, U. Giesen, A. Heiske, G. Feinberg, D. Hentschel, S. Hilpp, H. Leiste, T. Rauscher, and F.-K. Thielemann, Phys. Rev. C **84**, 015802 (2011).
[23] N. Özkan, A. Murphy, R. N. Boyd, A. L. Cole, M. Famiano, R. T. Güray, M. Howard, L. Şahin, J. J. Zach, R. deHaan, J. Görres, M. C. Wiescher, M. S. Islam, and T. Rauscher, Nucl. Phys. A **710**, 469 (2002).
[24] G. Gyürky, G. G. Kiss, Z. Elekes, Z. S. Fülöp, E. Somorjai, and T. Rauscher, J. Phys. G: Nucl. Part. Phys. **34**, 817 (2007).
[25] E. Skakun and V. Batij, Z. Phys. A **344**, 13 (1992).
[26] J. Kopecky and M. Uhl, Phys. Rev. C **41**, 1941 (1990).
[27] A. Gilbert and A. G. W. Cameron, Can. J. Phys. **43**, 1446 (1965).
[28] R. Capote, M. Herman, P. Obložinský, P. G. Young, S. Goriely, T. Belgya, A. V. Ignatyuk, A. J. Koning, S. Hilaire, V. A. Plujko, M. Avrigeanu, O. Bersillon, M. B. Chadwick, T. Fukahori, Z. G. *et al.*, Nucl. Data Sheets **110**, 3107 (2009).
[29] D. M. Brink, Nucl. Phys. **4**, 215 (1957).
[30] P. Axel, Phys. Rev. **126**, 671 (1962).
[31] A. Koning, S. Hilaire, and S. Goriely, TALYS 1.9, *A nuclear reaction program* user manual [https://tendl.web.psi.ch/tendl_2019/talys.html] (2017).
[32] A. Koning and J. Delaroche, Nucl. Phys. A **713**, 231 (2003).
[33] V. Avrigeanu, M. Avrigeanu, and C. Mănăilescu, Phys. Rev. C **90**, 044612 (2014).
[34] R. Kelmar, A. Simon, O. Olivas-Gomez, P. Millican, C. S. Reingold, E. Churchman, A. M. Clark, S. L. Henderson, S. E. Kelly, D. Robertson, E. Stech, and W. P. Tan, Phys. Rev. C **101**, 015801 (2020).
[35] W. H. Hastings, Biometrika **57**, 97 (1970).
[36] S. Goriely, F. Tondeur, and J. Pearson, At. Data Nucl. Data Tables **77**, 311 (2001).
[37] S. Goriely, S. Hilaire, and A. J. Koning, Phys. Rev. C **78**, 064307 (2008).
[38] S. Hilaire, M. Girod, S. Goriely, and A. J. Koning, Phys. Rev. C **86**, 064317 (2012).
[39] S. Goriely, Phys. Lett. B **436**, 10 (1998).
[40] D. Pena Arteaga and P. Ring, Phys. Rev. C **77**, 034317 (2008).
[41] M. Martini, S. Hilaire, S. Goriely, A. Koning, and S. Péru, Nucl. Data Sheets **118**, 273 (2014).
[42] J. P. Jeukenne, A. Lejeune, and C. Mahaux, Phys. Rev. C **16**, 80 (1977).